

The first mini quasar

Michael Kuhlen & Piero Madau

*Department of Astronomy and Astrophysics, University of California at Santa Cruz, Santa Cruz, CA 95064, U.S.A.
(e-mail: mqk@ucolick.org, pmadau@ucolick.org)*

ABSTRACT

We investigate the environmental impact of the first active galactic nuclei that may have formed ~ 150 Myr after the big bang in low-mass $\sim 10^6 M_{\odot}$ minihaloes. Using ENZO, an adaptive-mesh refinement cosmological hydrodynamics code, we carry out three-dimensional simulations of the radiative feedback from ‘mini quasars’ powered by intermediate-mass black holes. We follow the non-equilibrium multispecies chemistry of primordial gas in the presence of a point source of X-ray radiation, which starts shining in a rare high- σ peak at $z = 21$ and emits a power-law spectrum in the 0.2–10 keV range. We find that, after one Salpeter time-scale, the mini quasar has heated up the simulation box to a volume-averaged temperature of 2800 K. The mean electron and H_2 fractions are now 0.03 and 4×10^{-5} ; the latter is 20 times larger than the primordial value, and will delay the buildup of a uniform UV photodissociating background. The net effect of the X-rays is to reduce gas clumping in the IGM by as much as a factor of 3. While the suppression of baryonic infall and the photoevaporation of some halo gas lower the gas mass fraction at overdensities δ in the range 20–2000, enhanced molecular cooling increases the amount of dense material at $\delta > 2000$. In many haloes within the proximity of our mini quasar the H_2 -boosting effect of X-rays is too weak to overcome heating, and the cold and dense gas mass actually decreases. We find little evidence for an entropy floor in gas at intermediate densities preventing gas contraction and H_2 formation: we show, instead, that molecular cooling can affect the dynamics of baryonic material before it has fallen into the potential well of dark matter haloes and virialized. Overall, the radiative feedback from X-rays enhances gas cooling in lower- σ peaks that are far away from the initial site of star formation, thus decreasing the clustering bias of the early pregalactic population, but does not appear to dramatically reverse or promote the collapse of pregalactic clouds as a whole.

Key words: cosmology: theory – galaxies: active – methods: numerical – X-rays: general

1 INTRODUCTION

The first ‘seed’ black holes (BHs) that later grew to become the supermassive variety that power active galactic nuclei (AGNs) must have appeared at very early epochs, $z > 10$: this is in order to have had sufficient time to build up via gas accretion a mass of several $\times 10^9 M_{\odot}$ by $z = 6.4$, the redshift of the most distant quasars discovered in the *Sloan Digital Sky Survey* (Fan et al. 2003). The origin and nature of this seed population remain uncertain. Numerical simulations performed in the context of hierarchical structure formation theories show that the first stars (the so-called ‘Population III’) in the Universe formed out of metal-free gas in dark matter ‘minihaloes’ of mass above a few $\times 10^5 h^{-1} M_{\odot}$ (Abel, Bryan, & Norman 2000; Fuller & Couchman 2000; Yoshida et al. 2003; Reed et al. 2005) condensing from the rare high- σ peaks of the primordial density fluctuation field at $z > 20$, and were likely very massive (e.g. Abel, Bryan, &

Norman 2002; Bromm, Coppi, & Larson 2002; see Bromm & Larson 2004 for a recent review). Non-rotating very massive stars in the mass window $150 \lesssim m_* \lesssim 250 M_{\odot}$ are expected to disappear as pair-instability supernovae (Bond, Arnett, & Carr 1984) and leave no compact remnants. Stars with $40 \lesssim m_* \lesssim 150 M_{\odot}$ and $m_* \gtrsim 250 M_{\odot}$ are predicted instead to collapse to BHs with masses comparable to those of their progenitors (Fryer, Woosley, & Heger 2001). Barring any fine tuning of the initial mass function of Population III stars, intermediate-mass BHs – with masses above the 5–20 M_{\odot} range of known ‘stellar-mass’ holes – may then be the inevitable endproduct of the first episodes of pregalactic star formation (Madau & Rees 2001). Another route for the creation of more massive black hole seeds may be the formation – and subsequent collapse as a result of the post-Newtonian instability – of supermassive stars with $m_* \gg 10^3 M_{\odot}$ (see, e.g., Shapiro 2004a for a recent review) out of the lowest

angular momentum gas in rare haloes above the minimum mass for atomic cooling at high redshifts (Bromm & Loeb 2003; Koushiappas, Bullock, & Dekel 2004). Our simulations are related more closely to the former type of scenario.

Physical conditions in the central potential wells of gas-rich protogalaxies may have been propitious for BH accretion. In the absence of an H₂ photodissociating UV flux and of ionizing X-ray radiation, three-dimensional simulations of early structure formation show that the fraction of cold, dense gas available for accretion on to seed holes or star formation exceeds 20 per cent for haloes more massive than $10^6 M_\odot$ (Machacek, Bryan, & Abel 2003). There is also the possibility that the collapse of a rotating very massive star may lead to the formation of a massive BH and a ‘ready-made’ accretion disc (Fryer et al. 2001; Shapiro 2004b) that may provide a convenient source of fuel to power a ‘miniquasar’.

The presence of accreting BHs powering Eddington-limited miniquasars at such a crucial formative stage in the evolution of the Universe presents a challenge to models of the epoch of first light and of the thermal and ionization early history of the intergalactic medium (IGM), and serves as the main motivation of this paper. Feedback processes from the first stars and their remnants likely played a key role in reheating and structuring the IGM and in regulating gas cooling and star formation in pre-galactic objects. Energetic photons from miniquasars may make the low-density IGM warm and weakly ionized prior to the epoch of reionization breakthrough (Madau et al. 2004; Ricotti, Ostriker, & Gnedin 2005). X-ray radiation may boost the free-electron fraction and catalyze the formation of H₂ molecules in dense regions, counteracting their destruction by UV Lyman-Werner radiation (Haiman, Abel, & Rees 2000; Machacek et al. 2003). Or it may furnish an entropy floor to the entire IGM, preventing gas contraction and therefore impeding rather than enhancing H₂ formation (Oh & Haiman 2003). Photoionization heating may evaporate back into the IGM some of the gas already incorporated into haloes with virial temperatures below a few thousand kelvins (Barkana & Loeb 1999; Haiman, Abel, & Madau 2001; Shapiro, Iliev, & Raga 2004). The detailed consequences of all these effects is poorly understood.

In this paper, we describe the results of fully 3D Eulerian cosmological hydrodynamical simulations of the effect of the first miniquasars on the thermal properties of the high-redshift IGM. The focus of our investigation is not the modeling of the processes that lead to gas accretion on to BHs, but rather the radiative feedback of this population on their environment and on structure formation as a whole. Since their host haloes form from the collapse of rare density fluctuations, miniquasars powered by accreting BHs are expected to be strongly clustered and highly biased tracers of the underlying dark matter (DM) distribution. We use the adaptive mesh refinement (AMR) technique to home in, with progressively finer resolution, on the densest parts of the ‘cosmic web’. Rather than approximating radiation fields as isotropic, we study the impact of a point-source of X-ray radiation that starts shining in a rare high- σ peak at $z = 21$, before a universal ionizing background is actually established. The outline of this paper is as follows. In § 2 we describe our suite of numerical simulations. § 3 presents general results of the simulations, with and without X-rays,

and on the influence on the thermal and ionization state of the IGM of a non-uniform radiation field in the optically thin limit. We discuss the distance-dependent radiative feedback effect of a miniquasar on the amount of primordial gas that can cool and collapse, thus becoming available for star formation, in § 4. Finally, we present our conclusions in §5.

2 SIMULATIONS

High-resolution hydrodynamics simulations of early structure formation in Λ CDM cosmologies are a powerful tool to track in detail the thermal and ionization history of a clumpy IGM and guide studies of early reheating. We have used a modified version ENZO, an adaptive mesh refinement (AMR), grid-based hybrid (hydro+N-body) code developed by Bryan & Norman (see <http://cosmos.ucsd.edu/enzo/>) to solve the cosmological hydrodynamics equations, study the cooling and collapse of primordial gas in DM haloes, and simulate the large-scale effect of a miniquasar turning on at very high redshift. All the results shown below assume a Λ CDM world model with parameters $\Omega_M = 0.3$, $\Omega_\Lambda = 0.7$, $h = 0.7$, $\Omega_b = 0.05$, $\sigma_8 = 0.85$, and $n = 1$.

The primordial distribution of gas and DM is initialized in a comoving box of 1 Mpc on a side using the linear power spectrum of Eisenstein and Hu (1999). We first identify in a pure N-body simulation the Lagrangian volume of the most massive DM halo at $z = 25$. At this time its total mass is $7 \times 10^5 M_\odot$, corresponding to a 3.5 sigma peak in the density fluctuation field. Because its mass is comparable to the mass threshold for gas cloud formation by molecular cooling, this halo will likely harbor the first collapsed baryonic object in our simulated volume. It is this halo that we flag as the host of the first massive BH. We then generate new initial conditions centered around this density peak, consisting of two nested 128^3 static grids, of which the inner one covers the central 0.5 Mpc volume. The DM density field is also sampled with 128^3 particles in the inner region, leading to a mass resolution of $m_{\text{DM}} = 2000 M_\odot$. This ensures that haloes above the cosmological Jeans mass are well resolved at all redshifts $z < 21$. At $z = 15$, the five most massive haloes in the box have between 5×10^3 and 10^4 DM particles.

During the evolution from $z = 99$ to $z = 15$, refined (child) grids are introduced with twice the spatial resolution of the coarser (parent) grid. The AMR is restricted to the inner 0.5 Mpc and is triggered when a cell reaches a DM overdensity (baryonic overdensity) of 2.0 (4.0). This low overdensity refinement criterion has been shown to yield comparable results in equivalent simulations with ENZO and the smoothed particle hydrodynamics (SPH) code GADGET over the entire range of the dark halo mass function (O’Shea et al. 2005a). The region of interest is allowed to dynamically refine further to a total of 8 levels on a 128^3 top grid, resulting in a maximum dynamic range (ratio of box size to the smallest spatial scale that can be resolved) of 32,768 or a maximum resolution of 30 pc (comoving). At the end of a typical simulation, the code uses $\gtrsim 2.2 \times 10^7$ computational grid cells on $\gtrsim 9800$ grids, with a median number of cells per grid of 768. We have also carried out two simulations with identical initial conditions but increasing the number of allowed refinement levels to 10 (for a maximum dynamic range of 131,072) and adding artificial pressure sup-

Table 1. Summary of simulations.

Name	Spectrum	Energy range	z_{on}	Lifetime	Description
NoBH	—	—	—	—	Reference simulation without miniquasar
PL	power law	0.2-10 keV	21-17.5	45 Myr	Fiducial simulation with miniquasar
PLlong	power law	0.2-10 keV	21-15.5	90 Myr	Extended miniquasar lifetime
PLhard	power law	0.4-10 keV	21-17.5	45 Myr	Harder spectrum
MCD	multicolour disc + power law	—	21-17.5	45 Myr	Includes Lyman-Werner H ₂ -dissociating flux
NoBH10	—	—	—	—	Like NoBH but with 10 refinement levels and APS
PL10	power law	0.2-10 keV	21-17.5	45 Myr	Like PL but with 10 refinement levels and APS

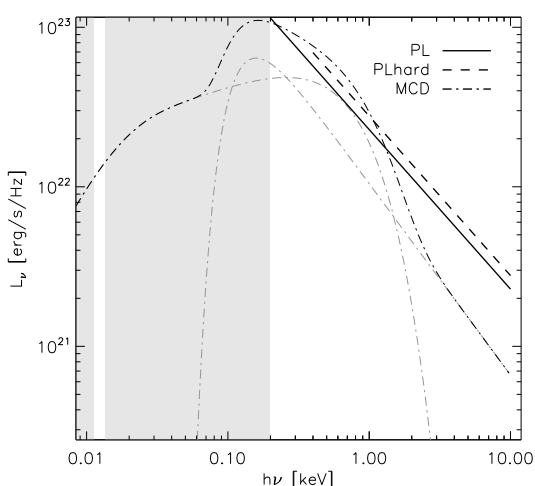


Figure 1. The three types of miniquasar spectra used in this paper. ‘PL’ (*solid*) and ‘PLhard’ (*dashed*) are simple power laws with $\alpha = 1$ and lower-energy cutoffs of 0.2 and 0.4 keV, respectively. ‘MCD’ (*dot-dashed*) is a combination of multicolour disc and $\alpha = 1.2$ power law. The two components are shown separately in light grey. In the MCD case only we have included radiation in the Lyman-Werner band (11.2 – 13.6 eV): photons between 13.6 eV and 0.2 keV are assumed to be absorbed within the emitting host halo. All spectra have been normalized to the Eddington luminosity of a $150 M_{\odot}$ black hole with radiative efficiency $\epsilon = 0.1$.

port (APS) to stabilize the density peaks that have reached maximal refinement against further collapse. Compared to the lower resolution simulations, these runs show only small deviations in the radial profiles of physical quantities within the inner regions of minihaloes (see discussion in § 3.3).

The spatial distribution of $128^3 \times 15/8$ collisionless dark matter particles determines at every time-step the large-scale gravitational field in the box. We evolve the non-equilibrium rate equations for nine species (H , H^+ , H^- , e , He , He^+ , He^{++} , H_2 , and H_2^+) in primordial self-gravitating gas, including radiative losses from atomic and molecular line cooling, Compton heating by X-rays and Compton cooling by the cosmic background radiation. The rate coefficients for the reaction network for these species are primarily those described in Abel et al. (1997): the H_2 cooling function is that of Lepp & Shull (1983). We impose the constraint that the minimum temperature attainable by radiative cooling is that of the cosmic microwave background.

A zero-metallicity progenitor star of mass $m_* =$

$150 M_{\odot}$ turning on at $z = 25$ in the host halo will emit $\gtrsim 10^{64}$ photons above 13.6 eV over a lifetime of 2.3 Myr (Schaerer 2002), about 10 such photons per halo baryon. The ensuing ionization front will overrun the host halo, photoevaporating most of the surrounding gas (Whalen, Abel, & Norman 2004). Gas accretion on to the BH remnants of the first stars that create H II regions may have to wait for new cold material to be made available through the hierarchical merging of many gaseous subunits. The simulations show that, by $z = 21$, our massive BH has been incorporated into a larger DM halo than contains 7 times more gas than the original host: it is at this time that we turn on the miniquasar radiation field. Our miniquasar is powered by a $m_{\text{BH}} = 150 M_{\odot}$ hole accreting at the Eddington rate and shining for 1 (2 in one of our 7 simulations) Salpeter time-scale, $t_S = 450 \epsilon / (1 - \epsilon)$ Myr, with a radiative efficiency of $\epsilon = 10$ per cent. Its exponentially growing mass and luminosity are recomputed at every time-step, and its trajectory is followed by flagging the DM particle corresponding to the maximum density in the host halo as our BH. The location of this flagged particle is determined at every time-step and used as the origin of an isotropic $1/r^2$ radiation field: from $z = 21$ to $z = 15$ our BH typically moves by less than 6 kpc (comoving). Note that, because of the considerable mass difference between our DM particle resolution ($2000 M_{\odot}$) and the initial mass of the black hole ($150 M_{\odot}$), we are not able to accurately track the true trajectory of the hole.

The photon energy distribution of putative high- z miniquasars is uncertain. The spectra of ‘ultraluminous’ X-ray sources in nearby galaxies appear to require both a soft component (well fit by a cool multicolour disc blackbody with $kT_{\text{max}} \simeq 0.15$ keV, which may indicate intermediate-mass BHs; Miller & Colbert 2004) and a non-thermal power-law component, $L_E \propto E^{-\alpha}$, of comparable luminosity and slope $\alpha \sim 1$. Here we have run simulations with three different spectra: one (‘PL’) assuming a simple power-law miniquasar spectrum with $\alpha = 1$ for photons with energies in the range 0.2 – 10 keV; one (‘PLhard’) with a similar spectrum, but with a low-energy cutoff of 0.4 keV; and one (‘MCD’) with luminosities equally divided between a multicolour disc component and a power law with $\alpha = 1.2$, both with a 0.2 keV low-energy cutoff. In the multicolour disc component, each annulus of a thin accretion disc is assumed to radiate as a blackbody with a radius dependent temperature, $T(r) \propto r^{-3/4}$, and the temperature of the innermost portion of the disc is related to the mass of the BH as $T_{\text{in}} \propto m_{\text{BH}}^{-1/4}$ (e.g. Makishima et al. 2000). All spectral energy distributions are normalized to the Eddington luminosity, which is exponentially increasing during the active phase of the

miniquasar. A plot of the different input spectra is shown in Fig. 1. For the MCD case only, we included in addition to the X-rays an H₂-dissociating flux in the Lyman-Werner band (LW, 11.2 – 13.6 eV), with an intensity determined by the Raleigh-Jeans tail of the multicolour disc. The implicit assumption for all of these spectra is that photons with energies between 13.6 eV and 0.2 keV are absorbed within the miniquasar host halo. For this reason our simulation is not strictly valid within the host halo, and we have excised it from all of the following analysis.

In the pre-reionization Universe, when the IGM is predominantly neutral, soft X-ray photons will be absorbed as they photoionize hydrogen or helium atoms. For a mixture of H and He with cosmic abundances, the effective bound-free absorption cross-section can be approximated to an accuracy of 30 per cent in the range 50 eV < $h\nu$ < 2 keV as $\sigma_{\text{bf}} \approx 4 \times 10^{-20} \text{ cm}^2 (h\nu/0.1 \text{ keV})^{-3}$. The mean free path of ionizing radiation in the neutral medium with overdensity $\delta \equiv \rho/\rho_b$ is then

$$\lambda = \frac{1}{n_{\text{H}} \sigma_{\text{bf}}} \approx 5 \text{ kpc} \left(\frac{1+z}{20} \right)^{-3} \left(\frac{h\nu}{0.1 \text{ keV}} \right)^3 \delta^{-1}. \quad (1)$$

Throughout the simulation box, gas at the mean density will be transparent to photons with energies > 0.2 keV and we take advantage of this by working in the optically thin approximation. At $z = 21$ even the most massive haloes in our simulation have total hydrogen columns below 10^{22} cm^{-2} , i.e. are transparent to photons above 0.7 keV. Since a power-law spectrum with $\nu I_{\nu} \sim \text{const}$ is characterized by equal power per logarithmic frequency interval, photoelectric absorption by intervening haloes will not significantly attenuate the ionizing energy flux: this is then only a function of distance from the miniquasar, and grows linearly with the mass of the hole in the PL and PLhard cases. Photoionizations and photodissociations couple the radiation field to the hydrodynamics through a heating term in the energy conservation equation and source and sink terms in the species abundance equations (Anninos et al. 1997). The radiative heating H_j and photoionization and photodissociation Γ_j rate coefficients are given by

$$H_j = \int_{\nu_{0,j}}^{\infty} \sigma_j(\nu) I(\nu) \frac{h\nu - h\nu_{0,j}}{h\nu} d\nu \quad (2)$$

$$\Gamma_j = \int_{\nu_{0,j}}^{\infty} \sigma_j(\nu) \frac{I(\nu)}{h\nu} d\nu, \quad (3)$$

where $\sigma_j(\nu)$ is the cross-section and $\nu_{0,j}$ is the frequency threshold for the j^{th} reaction, and $I(\nu)$ is the intensity of the radial radiation field.

3 GENERAL RESULTS

3.1 ‘NoBH’ simulation

A reference simulation with no radiation source (‘NoBH’) was run for comparison. The clustered structure around the selected high- σ peak of the density field is clearly seen in Fig. 2, a 3D volume rendering of the inner 0.5 Mpc box at redshifts 21 and 15.5. The figure shows gas at $4 < \delta < 10$, with the locations of dark matter minihaloes marked by spheres colored and sized according to their mass (the spheres are only markers, the actual shape of the haloes is

typically non-spherical). Several interleaving filaments are visible, at the intersections of which minihaloes are typically found. We identify the locations of DM minihaloes in the simulation volume by employing the HOP halo finder developed by Eisenstein & Hut (1998). This algorithm identifies haloes by grouping together particles that are associated with the same local density maximum, without enforcing spherical symmetry around the densest particle. We consider only haloes containing more than 100 particles. At $z = 21$, 55 haloes in our volume satisfy this criterion, by $z = 17.5$ this number has grown to 149, and by $z = 15.5$ to 262 haloes. At this epoch, only four haloes have reached the critical virial temperature for atomic cooling, $T_{\text{vir}} = 10^4 \text{ K}$, where

$$T_{\text{vir}} = 1.7 \times 10^4 \left(\frac{\mu}{1.2} \right) \left(\frac{M_{\text{halo}}}{10^7 h^{-1} \text{ M}_{\odot}} \right)^{2/3} \times \left[\frac{\Omega_M}{\Omega_M(z)} \frac{\Delta_{\text{vir}}}{18\pi^2} \right]^{1/3} \left(\frac{1+z}{20} \right) \text{ K}, \quad (4)$$

μ is the mean molecular weight, and Δ_{vir} is the density contrast at virialization.

The primordial fractional abundance of H₂ in the IGM is small, $x_{\text{H}_2} \approx 2 \times 10^{-6}$, as at $z > 100$ H₂ formation is inhibited because the required intermediaries, either H₂⁺ or H⁻, are destroyed by cosmic microwave background (CMB) photons (e.g. Galli & Palla 1998). Most of the gas in the simulation therefore cools by adiabatic expansion. Within collapsing minihaloes, however, gas densities and temperatures are large enough that H₂ formation is catalyzed by H⁻ ions through the associative detachment reaction H+H⁻ → H₂+e⁻, and the molecular fraction increases at the rate $dx_{\text{H}_2}/dt \propto x_e n_{\text{HI}} T_{\text{vir}}^{0.88}$, where x_e is the number of electrons per hydrogen atom. For $T_{\text{vir}} \lesssim$ a few thousand kelvins the virialization shock is not ionizing, the free electrons left over from recombination are depleted in the denser regions, and the production of H₂ stalls at a temperature-dependent asymptotic molecular fraction $x_{\text{H}_2} \approx 10^{-8} T_{\text{vir}}^{1.5} \ln(1+t/t_{\text{rec}})$, where t_{rec} is the hydrogen recombination time-scale (Tegmark et al. 1997). A typical H₂ fraction in excess of 200 times the primordial value is therefore produced after the collapse of structures with virial temperatures of order 10^3 K . This is large enough to efficiently cool the gas and allow it to collapse within a Hubble time unless significant heating occurs during this phase (Abel et al. 2000; Yoshida et al. 2003).

Fig. 3 (left panel) shows the fraction of cold gas within the virial radius as a function of halo mass for all the haloes identified at redshift 17.5. Note that the presence of halo masses below the HOP selection limit of $2 \times 10^5 \text{ M}_{\odot}$ is caused by differences between the extent of a halo as defined by the HOP algorithm and the virial radius measured by the spherically-averaged radial profile analysis. Following Machacek et al. (2001), we define f_c as the fraction of gas with temperature $< 0.5 T_{\text{vir}}$ and density > 1000 times the background (this is the halo gas that is able to cool below the virial temperature because of H₂), and f_{cd} as the fraction of gas with temperature $< 0.5 T_{\text{vir}}$ and (physical) density $> 10^{19} \text{ M}_{\odot} \text{ Mpc}^{-3}$ (this is the self-gravitating gas available for star formation). As in Machacek et al. (2001), we find that both f_c and f_{cd} are correlated with the halo mass, with the fraction of cold+dense gas increasing less rapidly than

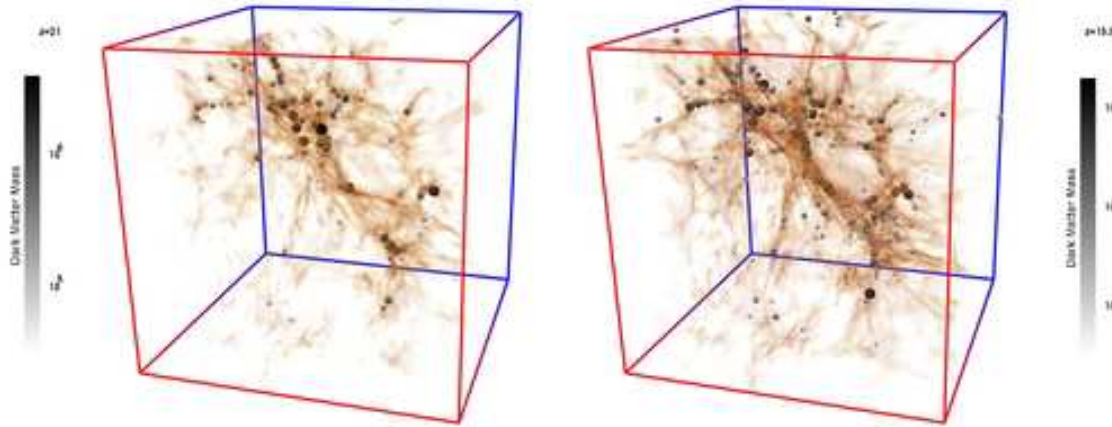


Figure 2. A 3D volume rendering of the IGM in the inner 0.5 Mpc simulated box at $z = 21$ and $z = 15.5$. Only gas with overdensity $4 < \delta < 10$ is shown: the locations of dark matter minihaloes are marked by spheres. The size and grey scale of the spheres indicate halo mass. At these epochs, the halo finder algorithm identifies 55 ($z = 21$) and 262 ($z = 15.5$) minihaloes within the simulated volume.

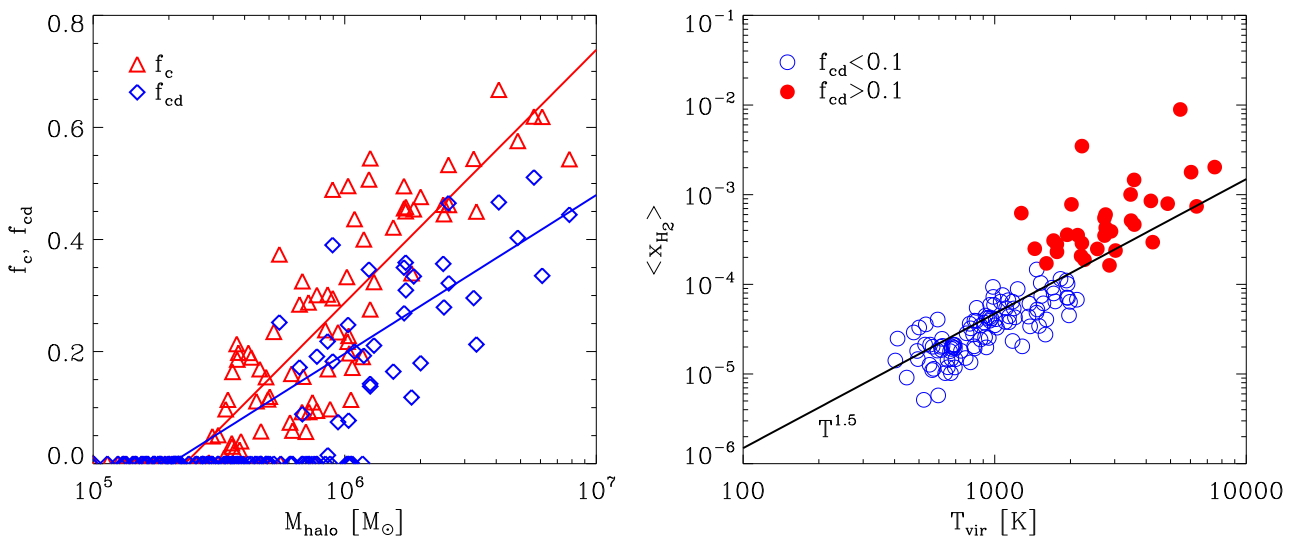


Figure 3. *Left:* Fraction of cold and cold+dense gas within the virial radius of all haloes identified at $z = 17.5$ with $T_{\text{vir}} > 400$, as a function of halo mass. *Triangles:* f_c , fraction of halo gas with $T < 0.5 T_{\text{vir}}$ and $\delta > 1000$ that cooled via roto-vibrational transitions of H_2 . *Diamonds:* f_{cd} , fraction of gas with $T < 0.5 T_{\text{vir}}$ and $\rho > 10^{19} \text{ M}_{\odot} \text{ Mpc}^{-3}$ that is available for star formation. The straight lines represent mean regression analyses of f_c and f_{cd} with the logarithm of halo mass. *Right:* Mass-weighted mean H_2 fraction as a function of virial temperature for all haloes at $z = 17.5$ with $T_{\text{vir}} > 400 \text{ K}$ and $f_{cd} < 0.1$ (empty circles) or $f_{cd} > 0.1$ (filled circles). The straight line marks the scaling of the temperature-dependent asymptotic molecular fraction.

f_c with M_{halo} . The mass threshold for significant baryonic condensation (non-zero f_{cd}) is approximately $5 \times 10^5 \text{ M}_{\odot}$ at these redshifts (Haiman, Thoul, & Loeb 1996). Also depicted in Fig. 3 (right panel) is the mass-weighted mean molecular fraction of all haloes with $T_{\text{vir}} > 400 \text{ K}$. Filled circles represent haloes with $f_{cd} > 0.1$, while open circles represent the others. The straight line marks the scaling of the asymptotic molecular fraction in the electron-depletion transition regime. Haloes with significant cold+dense gas fraction have larger $\langle x_{\text{H}_2} \rangle$ than those shown in fig. 3 of Yoshida et al. (2003). This is due to the high resolution attainable by an AMR code compared to SPH. The maximum gas density reached at redshift 15 in the most refined region of our sim-

ulation is $4 \times 10^5 \text{ cm}^{-3}$ (corresponding to an overdensity of 3×10^8): within this cold pocket the excited states of H_2 are in LTE and the cooling time is nearly independent of density (e.g. Lepp & Shull 1983).

At $z = 17.5$, ~ 90 per cent of the simulated volume contains gas with $T < 10 \text{ K}$, as shown by the differential temperature distributions in Fig. 4. The distribution of the entropy parameter $\kappa = kTn^{-2/3}$ is even more strongly peaked than the temperature distribution, as entropy is conserved during infall on to non-linear structures or Hubble expansion, which heat/cool the gas adiabatically. After decoupling from the CMB, the IGM temperatures drops as $T(z) \simeq 2.73(1 + z_d)[(1 + z)/(1 + z_d)]^2 \text{ K}$ for $z < z_d = 150$,

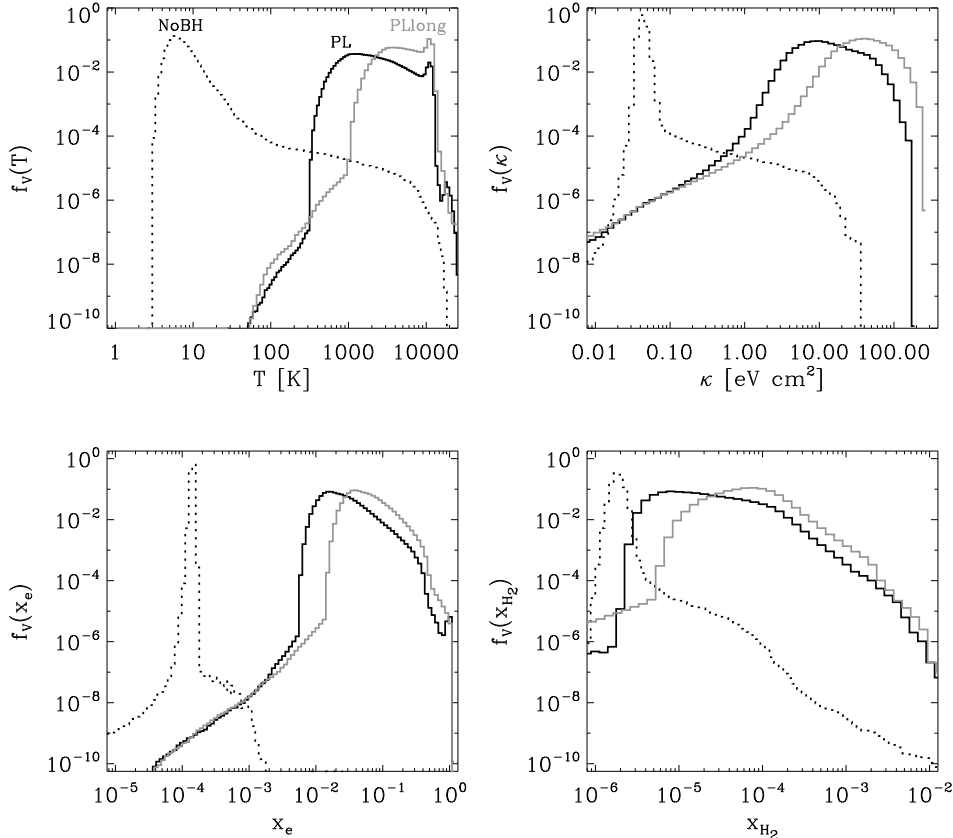


Figure 4. Distributions of temperature T , ‘entropy’ κ , electron fraction x_e , and molecular hydrogen fraction x_{H_2} (clockwise from upper left). *Dotted lines*: $z = 17.5$ NoBH run without miniquasar feedback. *Dark solid line*: $z = 17.5$ fiducial simulation, in which the miniquasar shines for one Salpeter time ($z = 21 - 17.5$). *Light solid line*: $z = 15.5$ PLong run, in which the miniquasar shines for two Salpeter times ($z = 21 - 15.5$). The volume-averaged temperature, entropy, electron fraction, and molecular fraction are (8 K, 0.04 eV cm², 1.4 × 10⁻⁴, 1.9 × 10⁻⁶), (2800 K, 17 eV cm², 0.03, 3.9 × 10⁻⁵), and (6150 K, 49 eV cm², 0.07, 9.3 × 10⁻⁵), respectively.

giving rise to an entropy floor of 0.04 eV cm², independent of redshift. Only gas that is shock heated during accretion on to DM haloes or that cools radiatively via H₂ can depart from this peak. Shock heating produces the extended tail out to $\kappa = 10$ eV cm² at a volume fraction in the range $f_V = 10^{-5} - 10^{-4}$. At these epochs, we find a collapsed gas mass fraction of $f_M = 2.5$ per cent. The fraction of baryons that gets shock heated ($\kappa > 0.1$ eV cm²) is $f_M = 6.7$ per cent. Radiative cooling processes affects such a tiny fraction of the volume that it remains outside the plotted range.¹ Due to the lack of ionizing sources the medium is almost completely neutral, with a distribution of electron fractions sharply peaked at $x_e = 1.5 \times 10^{-4}$. Note that the distribution of molecular hydrogen fraction, x_{H_2} , is considerably broader than that of x_e .

Another quantity of interest is the gas clumping factor $C = \langle n^2 \rangle / \langle n \rangle^2$, where the brackets denote volume-averaged quantities. The shorter radiative recombination time-scale, $t_{\text{rec}} = (\alpha \langle n_e \rangle C)^{-1}$ of a clumpy medium relative to a homogeneous one increases the total number of photons per

baryon required for reionization. We have calculated the average clumping factor within our simulation box of volume L^3 as

$$C = C_{\text{IGM}} + C_h = \sum_{\delta < 70} \frac{n_i^2 V_i}{\langle n_H \rangle^2 L^3} + \sum_{\delta > 70} \frac{n_i^2 V_i}{\langle n_H \rangle^2 L^3}, \quad (5)$$

where n_i is the number density of hydrogen in the i^{th} grid cell of volume V_i , $\langle n_H \rangle$ is the background hydrogen density, and the two sums are taken over all grid cells with baryonic overdensity smaller and larger than 70. We use this density threshold – corresponding to the mean baryonic overdensity at the virial radius of our haloes – to differentiate dense gas belonging to virialized haloes (C_h) and diffuse uncollapsed ‘intergalactic’ material (C_{IGM}). Gas within haloes only contributes to recombinations when it is photoionized: self-shielding of a cold gaseous disc and photoevaporation of halo gas by an external radiation field all make the contribution of dense material with $\delta \gtrsim 70$ to the overall clumping very uncertain (e.g. Haiman et al. 2001). In Fig. 5 we have plotted the evolution with redshift of C_{IGM} and C_h in the NoBH simulation. The clumping factor increases rapidly with time as structure formation progresses, with $C_{\text{IGM}} \approx 2.65 \exp[0.2(21 - z)]$ over the range in redshift we probe.

¹ The effect of radiative cooling can be observed in the ‘phase diagram’ of Fig. 6 as the bluish tail at $\delta > 100$, $T < 1000$ K, and volume fraction $f_V < 10^{-8}$.

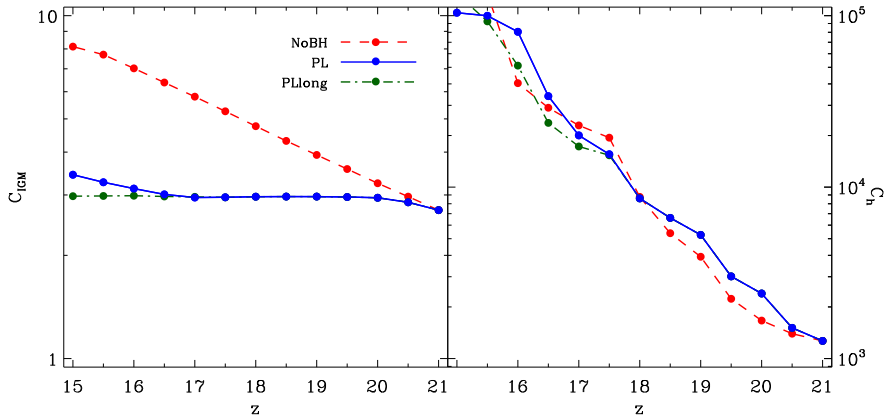


Figure 5. Clumping factor ($\langle n^2 \rangle / \langle n \rangle^2$) as a function of redshift for the NoBH, PL, and PLlong simulations. *Left:* Evolution of the clumping factor associated with diffuse ‘intergalactic’ ($\delta < 70$) material. *Right:* halo ($\delta > 70$) clumping factor. Note that this is not reduced in the presence of X-ray heating.

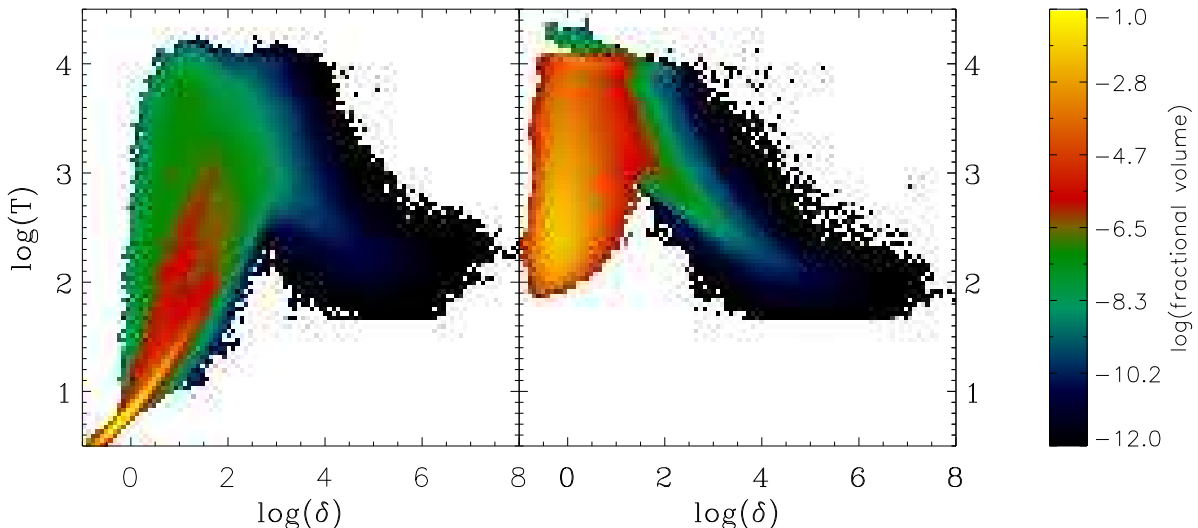


Figure 6. Two-dimensional distribution of gas temperature versus baryonic overdensity at $z = 17.5$. The color coding indicates the fraction of the simulated volume at a given (δ, T) . *Left:* NoBH run. *Right:* PL run.

3.2 Heating and ionization by the miniquasar

X-ray radiation from the miniquasar partially ionizes most of the gas in the simulated volume both by direct photoionization of H I and He I and indirectly by collisional ionization of H I by the fast photoelectrons. We have adopted the fitting formulae of Shull & van Steenberg (1985), cast as a function of the hydrogen ionized fraction, $x = n_{\text{H}^+} / n_{\text{H}}$, to determine the fraction of energy of a photoelectron deposited as heat versus further ionization. For photon energies above 0.2 keV, the ratio of the H I / He I photoionization cross-sections drops below 4 per cent: since the primordial ratio of helium to hydrogen is about 8 per cent, the photoionization and heating rates are dominated by helium absorption, which exceeds the hydrogen contribution by $\sim 2 : 1$. While He I is the main source of hot primary photoelectrons, however, it is H I that undergoes the bulk of secondary ionizations. A primary nonthermal photoelectron of energy $E = 1$ keV in a

medium with residual ionization fraction (from the recombination epoch) $x = 2 \times 10^{-4}$ will create over two dozens secondary electrons, depositing a fraction $f_1 = 0.37$ of its initial energy as secondary ionizations of H I, $f_2 = 0.05$ as secondary ionizations of He I, and $f_3 = 0.13$ as heat. The time-scale for electron-electron encounters resulting in a fractional energy loss $f = \Delta E / E$,

$$t_{\text{ee}} \approx 140 \text{ yr } E f \left(\frac{1+z}{20} \right)^{-3} \left(\frac{\ln \Lambda}{20} \right)^{-1} x^{-1} \delta^{-1} \quad (6)$$

(where E is measured in keV), is typically much shorter than the electron Compton cooling time-scale: the primary photoelectron will therefore ionize and heat the surrounding medium before it is cooled by the CMB. The fraction of primary energy going into heat increases gradually with x , reaching $f_3 = 0.5$ at $x = 0.04$. Secondary ionizations enhance the rates for ionization of H I and He I (but not for

He II , Shull & Van Steenberg 1985), and introduce an additional coupling between the abundance rate equations. The rate coefficients for H I and He I ionizations can be written as

$$\Gamma_{\text{HI}} + f_1(x) \left(H_{\text{HI}} + \frac{n_{\text{HeI}}}{n_{\text{HI}}} H_{\text{HeI}} \right) \frac{1}{13.6 \text{ eV}} \quad (7)$$

and

$$\Gamma_{\text{HeI}} + f_2(x) \left(H_{\text{HeI}} + \frac{n_{\text{HI}}}{n_{\text{HeI}}} H_{\text{HI}} \right) \frac{1}{24.6 \text{ eV}}, \quad (8)$$

respectively. We self-consistently evolve the hydrogen ionization fraction x and the hydrogen and helium abundances throughout the simulations (note that the Shull & van Steenberg fitting formulae were derived assuming equal ionization fractions of hydrogen and singly-ionized helium).

The two-dimensional distribution of gas overdensity and temperature at $z = 17.5$ is shown in Fig. 6 for the NoBH and PL simulations. The color coding in this phase diagram indicates the fraction of the simulated volume at a given (δ, T) . Most of the gas in the NoBH run lies on the yellow line ($\kappa = KTn^{-2/3}T = \text{const}$) representing the initial adiabat. At low overdensities the temperature either drops because of Hubble expansion or rises because of adiabatic compression until the gas is shock heated (red and green swath) to virial values, $T = 10^3 - 10^4 \text{ K}$. At higher densities, the blue cooling branch follows the evolutionary tracks in the temperature-density plane for spherically collapsing clouds (Yoshida et al. 2003). H_2 line emission lowers the temperature down to $\approx 100 \text{ K}$, the minimum value attainable by molecular cooling. The onset of the gravitational instability can further compress the gas and cause a modest rise in temperature again (Abel et al. 2000).

After shining for a Salpeter time-scale, the miniquasar has heated up the box to a volume-averaged temperature of 2800 K. The mean electron fraction and entropy are now 0.03 and 17 eV cm² (see Fig. 4): farther than 20 kpc (comoving) from the source hydrogen is never ionized to more than 30 per cent. Gas near the miniquasar is heated above 10⁴ K and quickly cools down via efficient atomic processes: the green finger at $\log \delta = 0, \log(T/\text{K}) > 4$ represents baryonic material in this phase. The increased electron fraction and gas temperature boost the gas-phase H_2 production, which occurs on a time-scale,

$$t_{\text{H}_2} = 30 \text{ Myr} \left(\frac{x_{\text{H}_2}}{10^{-5}} \right) \left(\frac{0.01}{x_e} \right) x_{\text{HI}}^{-1} T_3^{-0.88} \delta^{-1} \left(\frac{1+z}{20} \right)^{-3}, \quad (9)$$

that is much shorter than the hydrogen recombination time,

$$t_{\text{rec}} = 9 \times 10^3 \text{ Myr} \left(\frac{0.01}{x_e} \right) T_3^{0.64} \delta^{-1} \left(\frac{1+z}{20} \right)^{-3} \quad (10)$$

(here $T_3 \equiv T/10^3 \text{ K}$). The volume-averaged molecular fraction is now 20 times larger than the primordial value, with denser filaments in the IGM ($\delta \sim 10 - 20$) being traced out by a smaller electron fraction and by a molecular fraction in the range $10^{-5} - 10^{-3}$ (see Fig. 7). This large molecular fraction will hinder the buildup of a uniform UV photodissociating background, as the maximum optical depth of the IGM in the H_2 LW bands can now exceed 10 (cf. Ricotti, Gnedin, & Shull 2001; Haiman et al. 2000). It will also promote H_2 radiative cooling in filaments on a time-scale,

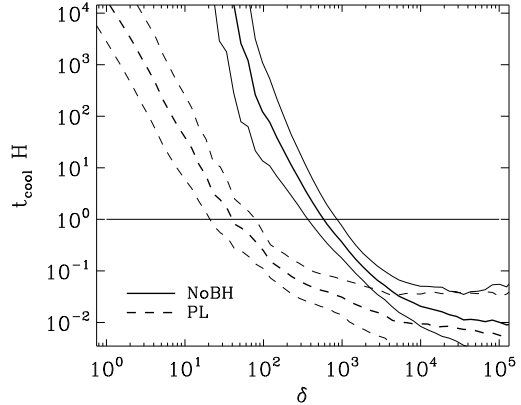


Figure 8. Mean H_2 cooling time (in units of H^{-1}) versus gas overdensity, for the NoBH (solid line) and PL (dashed line) runs at $z = 17.5$. The thin lines show departures of one root mean square ($((t_{\text{cool}}^2) - \langle t_{\text{cool}} \rangle^2)^{1/2}$) from the mean. Gas below the thin horizontal line can cool down in a Hubble time.

$$t_{\text{cool}} \approx 650 \text{ Myr} \left(\frac{10^{-3}}{x_{\text{H}_2}} \right) x_{\text{HI}}^{-1} \delta^{-1} \left(\frac{1+z}{20} \right)^{-3} e^{730 \text{ K}/T}, \quad (11)$$

(Machacek et al. 2001) that can be shorter than the Hubble expansion time, $1/H \simeq 285 \text{ Myr} [(1+z)/20]^{-3/2}$, and the Compton cooling time for mostly neutral primordial gas, $t_C = 8 \text{ Myr} x_e^{-1} [(1+z)/20]^{-4}$. In Fig. 8 we plot the mean H_2 cooling time in units of the expansion time-scale H^{-1} versus overdensity, at $z = 17.5$. In the NoBH simulation only gas with $\delta > 600$ can cool in a Hubble time. This critical cooling density is lowered to $\delta \approx 40$ in the PL simulation, due to the enhanced H_2 fraction. Molecular cooling can then affect the dynamics of baryonic material before it has fallen into the potential well of DM haloes and virialized. Gas in the simulation box is now able to collapse and cool more rapidly within subsequent star-forming minihaloes, without the need to produce much additional H_2 .

The global environmental impact of the miniquasar is illustrated in Fig. 9, where we plot in the top panel the volume (f_V) and mass fraction (f_M) as a function of overdensity in the NoBH and PL runs. The bottom panel shows the corresponding percentage change from the NoBH to the PL case ($100 \times (f_{\text{PL}} - f_{\text{NoBH}})/f_{\text{NoBH}}$). Three prominent features are clearly seen in this figure: 1) over most of the simulation volume, the net effect of X-rays is to reduce gas clumping due to the smoothing of sheets and filaments in the ‘cosmic web’ by gas pressure. This ‘Jeans smoothing’ removes gas from intermediate δ ’s and puffs it up to low overdensities ($\Delta f > 0$ for $1 < \delta < 10$), thereby filling in underdense regions ($\Delta f < 0$ for $\delta < 1$);² 2) the suppression of baryonic infall and the photoevaporation back into the IGM of some of the gas already incorporated into haloes both lower

² In the miniquasar simulations the IGM clumping factor remains approximately constant, $C_{\text{IGM}} \simeq 3$, from $z = 21$ to $z = 15$ (see the left panel in Fig. 5). Because of the decreasing background density with time, the IGM recombination time-scale at a given temperature therefore increases as $(1+z)^{-3}$ over this redshift interval.

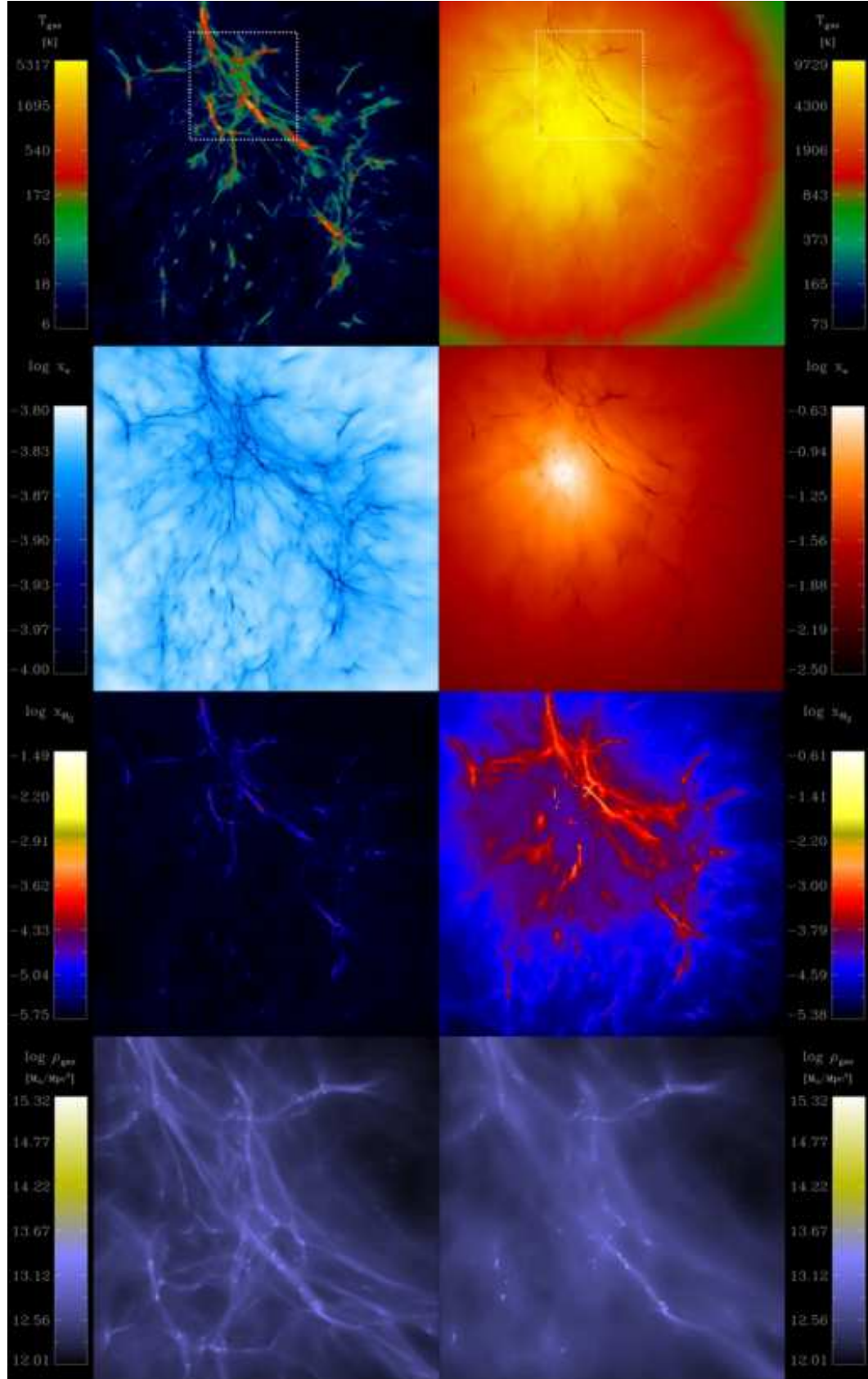


Figure 7. From top to bottom: Projected temperature, electron fraction, and molecular fraction distributions in the simulation box for runs NoBH (left) and PL (right) at $z = 17.5$. The bottom panel shows the projected gas density in a smaller 127 comoving kpc region (dotted outline in top panels) to highlight the effect of Jeans smoothing.

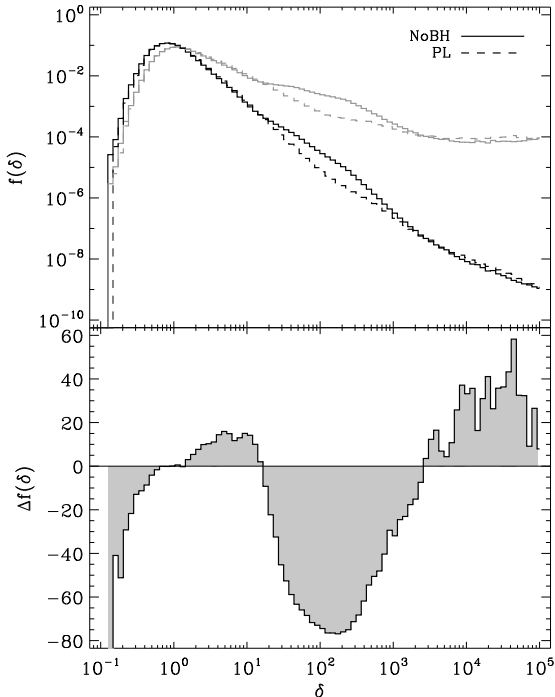


Figure 9. Top: volume (black lines) and mass (gray lines) fractions of gas overdensity $\delta = \rho/\rho_b$, in the NoBH (solid lines) and PL (dashed lines) simulations at $z = 17.5$. Bottom: Percentage change, $100 \times [f(\text{PL}) - f(\text{NoBH})]/f(\text{NoBH})$ in gas volume/mass fraction as a function of δ .

the gas mass fraction at $20 < \delta < 2000$; and 3) enhanced molecular cooling increases the amount of dense material at $\delta > 2000$. While the vast majority of the baryons, both in volume and mass, are heated up, the densest gas at the centres of haloes is actually cooled, due to the X-ray catalysis of molecular hydrogen. The feedback effect of X-rays on the formation and cooling of pregalactic minihaloes will be discussed in more details in the next section.

In the PLlong simulation we let the miniquasar shine for two Salpeter times, from $z = 21$ to $z = 15.5$, leading to a final black hole mass of $1100 M_\odot$. The increased intensity and duration of the radiation further enhances the effects described above (see Fig. 4). At $z = 15.5$, the volume averages in the box are: $\langle T \rangle = 6150$ K, $\langle \kappa \rangle = 49$ eVcm 2 , $\langle x_e \rangle = 0.07$, and $\langle x_{H_2} \rangle = 9.3 \times 10^{-5}$. The additional heating, however, does not further decrease the IGM clumping factor, and the halo clumping factor is still not affected (see Fig. 5). The increase in $\langle x_{H_2} \rangle$ by more than a factor of two is the most significant difference between the PL to PLlong simulation. This will make it even harder for subsequent generation of sources to establish a uniform Lyman-Werner background. Note that if early black holes undergo a period of super-Eddington mass growth (Volonteri & Rees 2005; Haiman 2004), a possible subsequent luminous miniquasar phase, powered by a more massive hole, might have feedback effects more similar to, or even exceeding those of our PLlong simulation.

4 X-RAY RADIATIVE FEEDBACK: POSITIVE OR NEGATIVE?

The impact of the radiation produced by Population III stars and their remnants on H₂ chemistry and the properties of star-forming gas in low-mass haloes has been studied by many authors. Molecular hydrogen is fragile and easily photodissociated by soft UV photons below 13.6 eV (e.g. Haiman, Rees, & Loeb 1997; Ciardi, Ferrara, & Abel 2000; Machacek et al. 2001; Glover & Brand 2001). While this negative feedback may suppress gas cooling and collapse, the formation of H₂ molecules is catalyzed by free electrons, and any process that increased their abundance would boost the abundance of H₂ as well. Fossil H II regions (Ricotti et al. 2001) and X-ray photons may provide such positive feedback (Haiman et al. 2000; Venkatesan, Giroux, & Shull 2001; Machacek et al. 2003; Glover & Brand 2003; Cen 2003). The issue of whether positive feedback processes dominate over negative feedback is still open. All we offer here is an assessment of the effect of X-rays in the absence of a strong photodissociating flux. This condition would naturally be fulfilled if accreting intermediate-mass BHs were the end-product of the first episodes of Population III star formation, as miniquasars are much more efficient sources of radiation than their stellar-progenitors (Madau et al. 2004). As already mentioned in § 2, our MCD run includes in addition to the X-rays a LW H₂-dissociating flux with an intensity determined by the Raleigh-Jeans tail of the multicolour disc, $I_{\text{LW}}(z = 21) = 10^{-21}$ ergs cm $^{-2}$ s $^{-1}$ Hz $^{-1}$ sr $^{-1}$ at a comoving distance of 7.2 kpc, which is 10 (3) times lower than the 0.2 keV (1 keV) X-ray flux (cf. Machacek et al. 2003). We find the results of the MCD simulation to be very similar to those of the PL run, and it is the latter that we analyze in detail below.

Fig. 10 depicts the change in halo gas content between the PL and NoBH simulations as a function of halo mass at two different epochs, $z = 17.5$ (when the miniquasar stops shining) and $z = 15.5$: haloes in the two simulations have been matched by location and DM mass. Different symbols represent total, cold, and cold+dense gas mass both for haloes closer than 75 comoving kpc from the radiation source and for those farther away. X-ray heating lowers the total gas mass in nearly all virialized DM clumps, both by photoevaporating baryons that were already incorporated into haloes and by suppressing baryonic infall into newly forming structures. This decrease in gas mass is more apparent below $M_{\text{halo}} \approx 10^6 M_\odot$, and it is the strongest in pregalactic clouds close to the miniquasars that have been exposed to the highest level of X-ray flux. Only a small fraction of the gas accreted by haloes in the NoBH run is retained by the host gravitational potential in the PL run. One of the potential wells that experiences the largest decrease in gas content is fairly massive, $M_{\text{halo}} = 10^6 M_\odot$, is located only 12 kpc (comoving) away from the miniquasar, and has a total gas fraction of 0.7 per cent, more than 20 times lower than in the NoBH simulation!

Population III stars, however, can only form from gas that is able to cool and condense. Fig. 11 shows the mass weighted mean H₂ fraction inside haloes in the PL simulation at $z = 17.5$ (cf. right panel of Fig. 3). Overall $\langle x_{H_2} \rangle$ increases by slightly more than one order of magnitude, independently of T_{vir} . Compared with the NoBH case, haloes

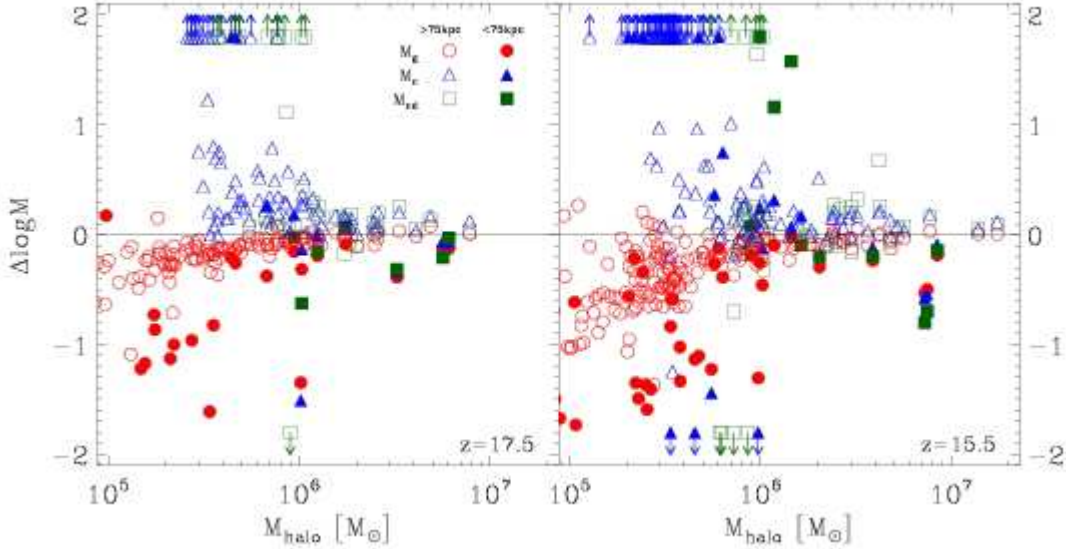


Figure 10. Variation in halo gas mass between the PL and NoBH simulations as a function of halo total mass (as measured in the NoBH run) at two different epochs. Symbols show $\log[M_i(\text{PL})/M_i(\text{NoBH})]$, with $i = g, c, cd$ for total gas, cold gas, and cold+dense gas mass. Filled symbols represent haloes within 75 comoving kpc of the miniquasars, empty symbols the others. Haloes with $|\Delta \log M_{c,cd}| > 2$ are shown as arrows at the top and bottom of the plot.

with $f_{cd} > 0.1$ can be found at slightly lower T_{vir} . None of the haloes with $T_{\text{vir}} < 800\text{K}$ has any cold+dense gas, even though their molecular fraction is quite high, $\langle x_{\text{H}_2} \rangle \approx 10^{-3}$. These haloes are the least massive haloes in our simulation and were formed only after the miniquasar began to shine. Continuous X-ray heating has prevented the gas from cooling and falling into the halo. As a consequence their mean gas mass fraction ($M_{\text{gas}}/M_{\text{tot}}$) is only 0.08 and their mean central temperature exceeds their virial temperature by a factor of 3. Haloes with larger T_{vir} , in contrast, formed earlier and their gas has contracted to densities where H_2 cooling is able to overcome X-ray heating.

Evidence for X-ray enhanced cooling is seen in many haloes above $2 \times 10^5 \text{ M}_\odot$. The largest relative increase in the amount of cold material occurs in the mass range $2 \times 10^5 < M_{\text{halo}} < 10^6 \text{ M}_\odot$, where the boosting effect can exceed 1-2 orders of magnitude! In this sense, X-ray pre-heating appears to somewhat decrease the threshold mass required for efficient gas cooling and star formation, albeit not by a large factor. In more massive peaks most baryons are already cold in the absence of X-rays (see Fig. 3), and positive feedback can only promote little additional cooling. Yet in many haloes in the proximity of our miniquasar the H_2 boosting effect of X-rays is too weak to overcome heating, and the cold and dense gas mass actually decreases. Table 2 summarizes the miniquasar's feedback effect on the total, cold, and cold+dense gas mass. We find evidence for a global positive feedback in minihaloes more than 75 comoving kpc away from the miniquasar, as the total mass in cold and cold+dense baryons increase by 30 and 44 per cent, respectively. Farther than 150 kpc this positive feedback is slightly larger yet, reaching +50 per cent for cold gas. Within 75 kpc of the miniquasar, however, the feedback is negative, as the total mass in cold+dense baryons decreases by more than 50 per cent. The total amount of gas mass in haloes is reduced at all distances within our simulated volume, with

Table 2. Summary of miniquasar feedback on halo total, cold, and cold+dense gas mass, at $z = 17.5$. All numbers are per cent change from NoBH to PL case.

	0.5Mpc box	< 75kpc	> 75kpc	> 150kpc
total	-20.5	-57.4	-10.5	-8.2
cold	+19.4	-43.4	+43.5	+49.3
cold+dense	+5.7	-52.1	+29.3	+38.4

haloes closer than 75 kpc losing on average more than half their gas mass. These effects are long-lasting, and persist at $z = 15.5$, 40 Myr after the miniquasar has stopped shining (see right panel of Fig. 10). Reducing the total amount of gas in the outer regions of haloes, while raising the amount of cold and dense gas available for star formation in the centres, could make it easier for these haloes to chemically enrich their surroundings.

Overall, however, positive and negative feedbacks nearly compensate each other, and the net impact of X-rays on the total amount of cold material available for star formation within the simulated volume is remarkably mild. By $z = 17.5$, exposure to X-ray radiation has boosted the total mass fractions of cold and cold+dense gas by only 14 and 6 per cent, respectively. There is hardly an X-ray 'sterilizing effect': star formation can proceed in minihaloes above the threshold mass, including those that are near the radiation source. In the most massive peaks at $z = 15.5$ the fraction of gas available for star formation in the NoBH control simulation is comparable to the value found when X-rays are present. Qualitatively similar conclusions were reached by Machacek et al. (2003), who showed that an early X-ray background cannot overcome the negative feedback from H_2 photodissociation by the soft UV radiation spectrum of the first stellar sources. Note that, at a distance of 50 comoving kpc, the X-ray flux from our miniquasars is comparable to the strongest X-ray background adopted by Machacek et al.

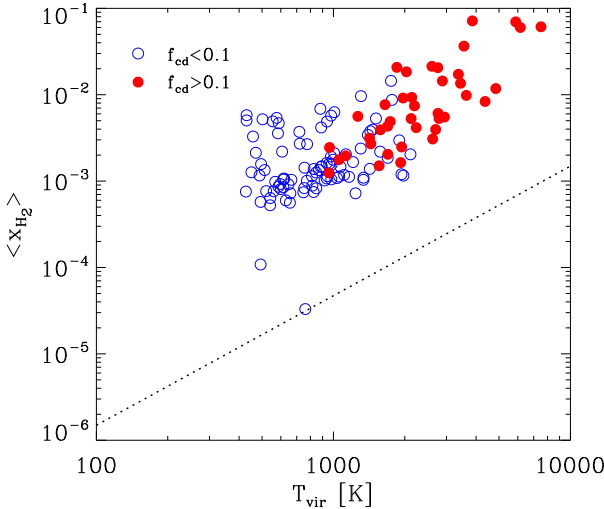


Figure 11. Same as Fig. 3 (right panel), but for the PL simulation. The dotted line is the $T^{1.5}$ line from the NoBH case.

(their $\epsilon_x = 10$ case). Here we find that, even in the absence of a strong LW flux, the radiative feedback from X-rays is subtle. It enhances gas cooling in lower- σ peaks that are far away from the initial site of star formation, thus decreasing the clustering bias of the early pregalactic population, but does not dramatically reverse or promote the collapse of pregalactic clouds as a whole.

It has been suggested recently by Oh & Haiman (2003) that an early X-ray background would establish an entropy floor over the entire IGM, thus preventing gas contraction, H_2 formation, cooling, and the build up of dense cores in minihaloes. The implication is a large reduction in the collapsed gas fraction and a pause in the cosmic star formation history, before more massive haloes with $T_{vir} > 10^4$ K (which can undergo atomic cooling) start forming. We find little evidence for preheating suppressing H_2 formation. None of our minihaloes exhibits an entropy floor and, as we have shown above, the amount of cold and dense gas in the centres is actually enhanced in haloes sufficiently removed from the miniquasar. Oh & Haiman considered the evolution of a pre-heated, isolated, uniform density gas parcel with initially primordial H_2 fraction, and showed that the entropy floor prevented subsequent H_2 formation. In our simulations, however, the heating source is also a catalyst of H_2 . This causes the H_2 cooling time to become shorter than the Hubble expansion time at $\delta > 40$ (see Fig. 8), and thus gas entropy is no longer a conserved quantity inside and in the vicinity of minihaloes.

Fig. 12 shows spherically averaged mass-weighted profiles of δ , T , κ , x_e and x_{H_2} at $z = 17.5$ of a typical low mass minihalo in our simulations. It has a dark matter mass of $3 \times 10^5 M_\odot$ ($T_{vir} \approx 925$ K), a virial radius of 127 pc (proper), and is located 200 comoving kpc from the miniquasar. In the NoBH simulation it has a total gas mass of $5.7 \times 10^4 M_\odot$, a cold gas mass of $1.1 \times 10^4 M_\odot$, and no cold+dense gas. The central regions of this halo have only triggered refinement down to level 7, one shy of the maximum refinement level. It has a central core, where the density profile lev-

els off at $\delta = 7000$. The gas temperature rises from about 100 K to T_{vir} at the virial radius, and then drops down to the central value of 350 K. This drop is possible due to the slightly elevated central H_2 fraction of 2.7×10^{-4} , which, however, is not high enough to allow the gas to condense to the cold+dense threshold density of 330 cm^{-3} in a Hubble time. The X-ray flux from the miniquasar changes this picture dramatically. The H_2 catalysis has led to an enhancement of almost 2 orders of magnitude in x_{H_2} outside the virial radius, from 10^{-5} to 8×10^{-4} . Towards the centre the increase in temperature and density allows the H_2 abundance to grow further, peaking at a central value of $x_{H_2} = 6.6 \times 10^{-3}$. This increase in x_{H_2} causes the gas to cool down to 140 K and greatly increases the central over-density ($\delta = 3 \times 10^5$), triggering refinement all the way to the maximum refinement level. In the PL simulation the external medium is at a temperature of $\gtrsim 3000$ K, which is much higher than T_{vir} . Thus no virial shock develops, and H_2 cooling causes the temperature profile to decrease monotonically towards the centre, dropping below T_{vir} at ~ 40 pc, a third of the virial radius. Gas that is hotter than T_{vir} cannot accrete on to the halo, and as a consequence the outer halo regions show a reduced gas density. The total gas mass decreases by 30 per cent down to $4.0 \times 10^4 M_\odot$. The increased cooling, however, has boosted the amount of cold gas by 60 per cent, up to $1.8 \times 10^4 M_\odot$, and even allowed $6.5 \times 10^3 M_\odot$ to reach the cold+dense threshold. The entropy profile reflects the additional cooling in the centre: it also decreases monotonically and reaches a minimum of $2.2 \times 10^{-4} \text{ eV cm}^2$, a factor of 30 below the central value in the NoBH case ($6.4 \times 10^{-3} \text{ eV cm}^2$).

5 DISCUSSION

Active galactic nuclei powered by supermassive holes keep the Universe ionized at $z \lesssim 4$, structure the IGM, and probably regulate star formation in their host galaxies. Their seeds were likely planted at very early epochs through the collapse of massive stars. Intermediate-mass holes accreting gas from the surrounding medium may shine as miniquasars at redshifts as high as $z \sim 20$. In this paper we have carried out AMR cosmological simulations using ENZO to address the thermodynamic effect of miniquasars on the IGM at early times.

X-ray radiation from the miniquasar efficiently heats the gas in the simulated box to a volume-averaged temperature of 2800 K after one Salpeter time ($z = 17.5$), and 6150 K after two ($z = 15.5$). The main effect of this sharp increase in temperature is a reduction of gas clumping in the IGM by as much as a factor of 3, due to the Jeans smoothing of sheets and filaments in the ‘cosmic web’ by increased gas pressure. This smoothing will lower the number of hydrogen recombinations and thus the number of UV photons per baryon required to reionize the universe. Since X-rays are more efficient at heating than at ionizing, the free electron fraction is never raised to more than ~ 10 per cent, reaching a volume average of 3 per cent at $z = 17.5$. Provided that either collisions or Ly α radiation can couple the spin temperature to the kinetic temperature of the largely neutral gas, it may be possible to observe the X-ray heated region in redshifted 21-cm line emission against the CMB (Madau,

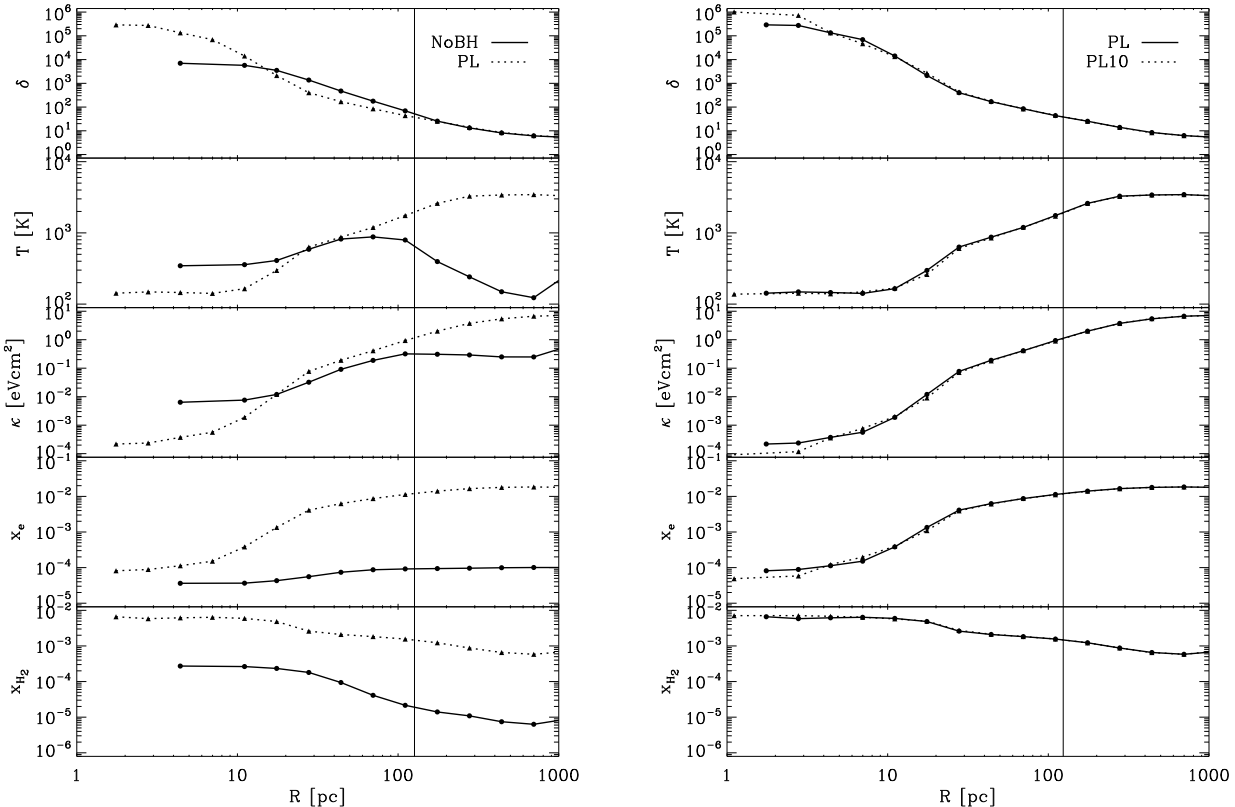


Figure 12. Spherically averaged mass-weighted radial profiles of δ , T , κ , x_e , and x_{H_2} of a representative halo at $z = 17.5$. In the left panel we compare the NoBH with the PL case, in the right panel the PL with the PL10 case. This halo has a DM mass of $3 \times 10^5 M_\odot$ and is located 200 comoving kpc from the miniquasar. See text for discussion.

Meiksin, & Rees 1997) with future facilities like the *Low Frequency ARray (LOFAR)*.

The elevated free electron fraction leads to a strong enhancement of molecular hydrogen, both inside haloes and in the more tenuous filaments. The volume-averaged H_2 fraction is raised to $x_{H_2} = 4 \times 10^{-5}$, 20 times larger than the primordial value. This will delay the buildup of a uniform UV photodissociating background by subsequent sources of Lyman-Werner photons. We plan to carry out a detailed calculation of this suppression and its consequences in future work. The increased H_2 abundance allows gas with over-densities $\delta > 40$ to cool within a Hubble time. As a consequence the evolution of gas within haloes and filaments is not adiabatic, and no entropy floor is established. While global heating suppresses baryonic infall and lowers the gas mass fraction at over-densities δ in the range 20-2000, enhanced molecular cooling increases the amount of dense material at $\delta > 2000$. Thus, while the vast majority of the baryons, both in volume and mass, is heated up, the densest gas at the centres of haloes is actually cooled down. The largest relative increase in the amount of cold material occurs in the mass range $2 \times 10^5 < M_{\text{halo}} < 10^6 M_\odot$, where the boosting effect can exceed 1-2 orders of magnitude. Yet for many haloes in the proximity of our miniquasar (< 75 kpc) the

H_2 -boosting effect is too weak to overcome heating, and the cold and dense gas mass actually decreases. Overall, the radiative feedback from X-rays enhances gas cooling in lower- σ peaks that are far away from the initial site of star formation, thus decreasing the clustering bias of the early pregalactic population, but does not appear to dramatically reverse or promote the collapse of pregalactic clouds as a whole.

The spatial resolution of our AMR simulations is determined by the maximum refinement level, which is usually set by computational costs. Mesh cells that have refined down to the maximum refinement level can pose a problem. The physics of cooling and collapsing gas is inherently unstable: Jeans unstable cells should refine further, but the simulation does not allow it. This leads to an error in the numerical solution of the differential equations governing the system. One way to prevent the gas from continuing to trigger refinement is to introduce Artificial Pressure Support (APS). With APS the internal gas energy of every mesh cell that reaches maximum refinement and is Jeans unstable is raised to 10 times the value that would stabilize it against gravitational collapse. This provides support against further refinement, but comes at the cost of introducing an artificially high central pressure and temperature inside haloes that have reached maximum refinement. Neither applying APS

nor letting the simulation progress without it is correctly modelling the physics of the problem. The only solution is to continue to refine further (Abel et al. 2002) or to introduce sink particles (Krumholz, McKee, & Klein 2004). In our fiducial simulations we have 50,000-60,000 mesh cells at the maximum refinement level of 8. In order to determine whether the associated numerical error affects the conclusions of our study, we have run another set of NoBH and PL simulations from $z=21$ to $z=17.5$, with a maximum refinement level of 10 and APS. In the right panel of Fig. 12 we plot for the PL and PL10 runs a comparison of the five profiles described above. As expected the two profiles agree excellently at radii outside of the central core (> 10 pc). Even inside the core, the temperature and x_{H_2} profiles agree very well. The gas in the PL10 halo, however, has been able to reach an overdensity a factor of ~ 3.5 higher than in the PL case, and has ~ 50 per cent more cold+dense gas. Although we show here only profiles for one halo, we see similar trends for all haloes that reach maximum refinement, and so we conclude that the amount of cold+dense gas in haloes in the PL simulation should be viewed as a lower limit. The numerical error due to evolving the simulation with cells at the maximum refinement level is unlikely to affect the global conclusions of this paper.

While we have included the essential physics necessary to model the radiative feedback from the first miniquasars, our study, like any, has its limitations. In the following we briefly address some of these:

1) We have not considered the environmental impact of the progenitor of the black hole. In the case of direct collapse of a primordial gas cloud to an intermediate-mass black hole the issue of a progenitor star would not arise. The more typical formation mechanism of the black hole, however, may be the collapse of a Population III star. In this case the copious UV radiation emitted during its main-sequence lifetime could have significantly altered the initial conditions for our simulation. Recent three-dimensional simulations (O'Shea et al. 2005b) seem to indicate that the heating and ionizing effect from the Population III progenitor are rather short lived. In their simulation the gas quickly recombines and cools, H_2 reforms, and gas is able to collapse to form a second generation star in a neighboring halo only 265 pc from the Population III host halo.

2) The strong increase in H_2 abundance catalyzed by the X-rays is dependent on the absence of a Lyman-Werner H_2 -dissociating background. As shown by Machacek et al. (2003) the positive feedback effects from an X-ray background in the presence of a LW background are rather mild, and they did not find a global increase in H_2 abundance by a factor of 20. For this reason our work should be considered as a simulation of the *first* miniquasar in its volume, i.e. before other sources establish a LW background. How soon after the miniquasar a LW background can be established, given the large increase in H_2 , remains to be seen.

3) Recently there has been a renewed interest in the importance of deuterium hydride (HD) to the cooling of primordial gas clouds (Johnson & Bromm 2005; Lipovka, Nunez-Lopez, & Avila-Reese 2005; Nagakura & Omukai 2005). HD becomes more efficient than H_2 cooling at $T < 200K$, and, given a sufficient HD abundance, can cool gas down to below 100 K. In our simulations deuterium chem-

istry has been neglected. An increased free-electron fraction, as produced by our miniquasar, would lead to a catalysis of HD molecules, so it is quite possible that HD cooling may become important in the cores of our minihaloes.

4) As the emission spectrum of a miniquasar is uncertain, so are the photoheating and photoionization rates. We have mainly considered a pure power-law spectrum, ranging from 0.2 to 10 keV, with a slope of -1 . The power-law component in our MCD simulation is slightly softer ($\alpha = -1.2$), but the differences between PL and MCD are negligible. In the PLhard simulation (lower cutoff of 0.4 keV), however, the miniquasar is much less effective. At $z = 17.5$ the volume-averaged temperature is only ~ 400 K, with $\langle x_e \rangle = 0.005$ and $\langle x_{H_2} \rangle = 6.7 \times 10^{-6}$. Note also that we have neglected UV radiation with $13.6\text{ eV} < h\nu < 200\text{ eV}$. If a significant amount of the emitted Lyman-continuum flux escapes the host halo, it will be necessary to follow the radiative transfer in order to fully assess the environmental influence of the first miniquasars.

5) We have not taken into account the possibility of a feedback effect from the miniquasar's radiation on the black hole's mass accretion rate. Instead of assuming a constant exponential growth rate, it would be better to determine \dot{M} as a function of time from the amount of cold gas available for accretion. Unfortunately our simulations don't resolve the length scale of the accretion flow, and a self-consistent treatment of the mass accretion rate will have to wait for higher resolution studies.

ACKNOWLEDGMENTS

We thank T. Abel, G. Bryan, Z. Haiman, and B. O'Shea for many informative discussions, and Ryan Montgomery for help with the phase diagrams. Fig. 2 was created with Nick Gnedin's *Ionization Front Interactive Tool* (IFRIT). Support for this work was provided by NSF grants PHY99-07949 and AST02-05738, and by NASA grants NAG5-11513 and NNG04GK85G (P.M.). P.M. acknowledges support from the Alexander von Humboldt Foundation. M.K. thanks the Graduate Fellowship Program at Kavli Institute for Theoretical Physics, Santa Barbara, where part of this work was done. All computations were performed on NASA's Project Columbia supercomputer system and on UpsAnd, a Beowulf cluster at UCSC. Movies of the simulations are available at <http://www.ucolick.org/~mqk/miniqso>.

REFERENCES

- Abel, T., Anninos, P., Zhang, Y., Norman, M. L., 1997, *New Astron.*, 2, 181
- Abel, T., Bryan, G., Norman, M. L., 2000, *ApJ*, 540, 39
- Abel, T., Bryan, G., Norman, M. L., 2002, *Science*, 295, 93
- Anninos, P., Zhang, Y., Abel, T., Norman, M. L., 1997, *New Astron.*, 2, 209
- Barkana, R., Loeb, A., 1999, *ApJ*, 523, 54
- Bond, J. R., Arnett, W. D., Carr, B. J., 1984, *ApJ*, 280, 825
- Bromm, V., Coppi, P. S., Larson, R. B., 2002, *ApJ*, 564, 23
- Bromm, V., Loeb A., 2003, *ApJ*, 596, 34
- Bromm, V., Larson, R. B., 2004, *ARA&A*, 42, 79
- Cen, R., 2003, *ApJ*, 591, 12
- Ciardi, B., Ferrara, A., Abel, T., 2000, *ApJ*, 533, 594
- Eisenstein, D. J., Hu, W., 1999, *ApJ*, 511, 5

Eisenstein, D. J., Hut, P., 1998, ApJ, 498, 137
 Fan, X., et al., 2003, ApJ, 125, 1649
 Fryer, C. L., Woosley, S. E., Heger, A., 2001, ApJ, 550, 372
 Fuller, T. M., Couchman, H. M. P., 2000, ApJ, 544, 6
 Galli, D., Palla, F., 1998, A&A, 335, 403
 Glover, S. C. O., Brand, P. W. J. L., 2001, MNRAS, 321, 385
 Glover, S. C. O., Brand, P. W. J. L., 2003, MNRAS, 340, 210
 Haiman, Z., 2004, ApJ, 613, 36
 Haiman, Z., Abel, T., Madau, P., 2001, ApJ, 551, 599
 Haiman, Z., Abel, T., Rees, M. J., 2000, ApJ, 534, 11
 Haiman, Z., Thoul, A. A., Loeb, A., 1996, ApJ, 464, 523
 Haiman, Z., Rees, M. J., Loeb, A., 1997, ApJ, 476, 458
 Johnson, J. L., Bromm, V., 2005, MNRAS, submitted
 (astro-ph/0505304)
 Koushiappas, S. M., Bullock, J. S., Dekel, A., 2004, MNRAS, 354,
 292
 Krumholz, M. R., McKee, C. F., Klein R. I., 2004, ApJ, 611, 399
 Lepp, S., Shull, J. M., 1983, ApJ, 270, 578
 Lipovka, A., Nunez-Lopez, R., Avila-Reese, V., 2005, MNRAS,
 in press (astro-ph/0503682)
 Machacek, M. M., Bryan, G. L., Abel, T., 2001, MNRAS, 548,
 509
 Machacek, M. M., Bryan, G. L., Abel, T., 2003, MNRAS, 338,
 273
 Madau, P., Meiksin, A., Rees, M. J., 1997, 475, 429
 Madau, P., Rees, M. J., 2001, ApJ, 551, L27
 Madau, P., Rees, M. J., Volonteri, M., Haardt, F., Oh, S. P., 2004,
 ApJ, 606, 484
 Makishima, K., et al. , 2000, ApJ, 535, 632
 Miller, M. C., Colbert, E. J. M., 2004, IJMPD, 13, 1
 Nagakura T., Omukai, K., 2005, MNRAS, submitted
 (astro-ph/0505599)
 Oh, S. P., Haiman, Z., 2003, MNRAS, 346, 456
 O'Shea, B. W., Nagamine, K., Springel, V., Hernquist, L., Norman, M. L., 2005a, ApJ, in press (astro-ph/0312651)
 O'Shea, B. W., Abel T., Whalen D., Norman M. L., 2005b, ApJ,
 in print (astro-ph/0503330)
 Reed, D. S., Bower, R., Frenk, C. S., Gao, L., Jenkins, A.,
 Theuns, T., White, S. D. M., 2005, MNRAS, submitted
 (astro-ph/0504038)
 Ricotti, M., Gnedin, N. Y., Shull, J. M., 2001, ApJ, 560, 580
 Ricotti, M., Ostriker, J. P., Gnedin, N. Y., 2005, MNRAS, 357,
 207
 Schaefer, D., 2002, A&A, 382, 28
 Shapiro, S. L., 2004a, in Carnegie Observatories Astrophysics Series, Vol 1: Coevolution of Black Holes and Galaxies, ed. L. C. Ho (Cambridge: Cambridge Univ. Press), p.103
 Shapiro, S. L., 2004b, ApJ, 610, 913
 Shapiro, P. R., Iliev, I. T., Raga, A. C., 2004, MNRAS, 348, 753
 Shull, J. M., Van Steenberg, M. E., 1985, ApJ, 298, 268
 Tegmark, M., Silk, J., Rees, M. J., Blanchard, A., Abel, T., Palla,
 F., 1997, ApJ, 474, 1
 Venkatesan, A., Giroux, M. L., Shull, M. J., 2001, ApJ, 563, 1
 Volonteri, M., Rees, M. J., 2005, ApJ, submitted
 (astro-ph/0506040)
 Whalen, D., Abel, T., Norman, M. L., 2004, ApJ, 610, 22
 Yoshida, N., Abel, T., Hernquist, L., Sugiyama, N., 2003, ApJ,
 592, 645